JOURNAL OF Materials CHEMISTRY

Nanohybrids of non-stoichiometric zinc ferrite in amorphous silica

Z. H. Zhou,[a] J. Wang,*[a] J. M. Xue[a] and H. S. O. Chan[b]

[a]*Department of Materials Science, Faculty of Science, National University of Singapore, Singapore 119260. E-mail: maswangj@nus.edu.sg*
[b]*Department of Chemistry, Faculty of Science, National University of Singapore, Singapore 119260*

Received 20th June 2001, Accepted 3rd September 2001
First published as an Advance Article on the web 31st October 2001

Nanohybrids containing non-stoichiometric zinc ferrite of spinel structure in an amorphous silica matrix exhibit a fundamentally different structure to that formed by stoichiometric zinc ferrite. A unique cluster glass structure, where nanocrystallites of zinc ferrite exist in amorphous Fe-rich pockets, occurred at the significantly high Fe/Zn molar ratio of 10, as supported by the magnetic behaviour and characterisation by XRD and TEM. The occurrence of zinc ferrite crystallites due to the Zn^{2+} deficiency, together with the confinement of the silica matrix, suppresses the nucleation and crystallisation of α-Fe_2O_3 to a temperature above 900 °C, preserving the cluster glass structure. The Fe/Zn molar ratio also affects the optical properties of nanohybrids consisting of the zinc ferrite nanophase in amorphous silica, which demonstrate a high absorption coefficient to yellow light. The absorption edge was blue-shifted by 0.25 eV when the Fe/Zn ratio was increased from 2 to 10.

I Introduction

In recent years, there has been a growing demand for novel functional and transparent materials for non-linear optical devices, solid-state laser amplifiers and as transparent magnets. In particular, transparent magnets show great promise for magneto-optical recording, displays and holograms, as well as for magneto-optical solid devices in light waveguides or photonic circuits, such as isolators, modulators and switches.[1–3] By incorporating nanophase magnetic particles into a polymer, glass or ceramic matrix, functional nanohybrids with many interesting optical and magnetic properties have been successfully synthesised.[4–8] In these nanohybrids, transparency is affected by the absorption coefficients of both the magnetic nanoparticles and the matrix, as well as the configuration of their interfaces. The matrix phase also acts to control the *in situ* formation and coarsening of nanoparticles during processing, minimising the optical scattering observed with embedded coarse particles and therefore enhancing the transparency.

Iron oxides, such as Fe_3O_4 and γ-Fe_2O_3, are the magnetic phases that have been commonly employed in transparent magnetic nanocomposites. The range of matrix materials used is rather broad, extending from ion-exchange resins through polymeric waxes and polymer films to silica glass.[4–9] Nanocomposites employing silica as a matrix have been studied recently by several research groups.[7,8,10–14] For example, Monte *et al.*[7] investigated the growth mechanism of γ-Fe_2O_3 nanoparticles in a silica network and concluded that the reduction-oxidation reaction occurring at the surface of pores within the silica gel gave rise to the formation of γ-Fe_2O_3 nanoparticles. Cannas *et al.*[11] studied a similar composition and showed that both a high calcination temperature and a high iron concentration could reduce the overall saturation magnetisation. Nanophase $NiFe_2O_4$ in a silica matrix was synthesised by Li *et al.*,[14] who investigated both the formation mechanism and magnetic properties of the nanohybrid. However, these researchers did not study the optical properties of the nanocomposites. One of the very apparent reasons for this is the difficulty of preventing the formation of cracks and large pores in silica gel during thermal annealing. As a result, these previous studies were generally conducted on powdered specimens, making it impossible to measure their optical properties. In fact, most of the studies on the optical properties of silica composites involved mixing silica gel with pre-synthesised magnetic particles. For example, Bentivegna and co-workers[8,10] attempted to study the magnetic and optical properties of silica gel that was prepared by mixing an aqueous ferrofluid containing γ-Fe_2O_3 with a silica sol, followed by gelation. Since the nanophase γ-Fe_2O_3 was not formed *in situ* and was introduced into the gel structure in the form of a ferrofluid, its concentration and distribution could not be controlled properly, resulting in an overall saturation magnetisation of as low as 0.38 emu g^{-1}. Yasumori *et al.*[3] also introduced pre-synthesised Fe_3O_4 particles into a silica sol that was gelled at 60 °C,[3] resulting in a low Fe_3O_4 loading (5.58×10^{-3} mol%) and structural features in the micrometer scale, instead of the designed nanometer scale.

Recently, nanohybrids containing up to 30 wt% $ZnFe_2O_4$ nanoparticles in amorphous silica formed *in situ* were successfully synthesised in our laboratories.[15] Through careful control of several processing parameters, the bulk nanohybrids obtained have dimensions which are sufficiently large to permit investigation of their magnetic and optical properties. In this paper, we report the unique microstructure and magnetic and optical properties of nanohybrids consisting of non-stoichiometric zinc ferrite in a silica matrix obtained by deliberately increasing the Fe/Zn molar ratio to 10. On the basis of XRD, TEM, Raman and magnetic behaviour studies, the formation process of a unique cluster structure in the nanohybrids is discussed.

II Experimental details

1 Starting materials

The starting chemicals used in this study were: iron nitrate [$Fe(NO_3)_3 \cdot 9H_2O$] of reagent grade with purity > 99% (Fisher Scientific); zinc nitrate [$Zn(NO_3)_2 \cdot 6H_2O$] of purity > 98% (Goodrich Chemical Enterprise) and tetraethyl orthosilicate (TEOS) of purity > 98% (Aldrich Chemical Company, Inc.).

 DOI: 10.1039/b105427a

2 Experimental procedure

The zinc ferrite–silica nanohybrids chosen for this study were prepared by mixing TEOS, ethanol (EtOH) and an aqueous solution of mixed iron nitrate and zinc nitrate with the TEOS : EtOH : H_2O molar ratio being set at 1 : 1 : 5; the Fe/Zn ratio was adjusted by controlling the amount of iron nitrate and zinc nitrate added to the aqueous solution. An appropriate amount of EtOH was first mixed with the aqueous solution of mixed iron nitrate and zinc nitrate, followed by the slow addition of TEOS. The mixture appeared initially turbid and then turned transparent with emission of heat upon several minutes of vigorous stirring, indicating that hydrolysis of the TEOS had taken place. The clear mixture was then transferred into a covered plastic petric dish and left for slow gelation, which was accompanied by a volume shrinkage. Extra care was taken to prevent cracking of the gelled specimens by mechanical movement and vibration. The alcogels were then place into an oven for further drying at 150 °C for 24 h before they were heated to a designated annealing temperature in a furnace for 3 h to form the zinc ferrite–SiO_2 nanohybrids. In the following discussion, the notation ZF_xO-*n* will be used, where *n* indicates the annealing temperature and *x* the Fe/Zn molar ratio.

3 Characterisation

The zinc ferrite–silica nanohybrids were characterised for phases using both powder X-ray diffraction (Cu-Kα, Phillips PW1729 X-ray diffractometer) and Raman spectrometry (Renishaw 2000 micro-Raman system). The Raman spectrometer was operated in the backscattering geometry with a helium–neon laser operating at 632.8 nm as the excitation source. A transmission electron microscope (TEM, JEOL-100CX) was employed for studies of morphologies and microstructures of the nanophase zinc ferrite in silica. An FT-IR spectrometer (Bio-rad, FTS 135) was used to investigate the phase evolutions with increasing annealing temperature. The magnetic and optical properties were measured using a vibrating sample magnetometer (VSM, 41719.7, Oxford Instruments) and a UV-visible spectrophotometer (UV-1601, Shimadzu), respectively.

III Results and discussion

The morphology and distribution of nanoparticles in the silica matrix and their nanostructures were studied using transmission electron microscopy (TEM). Fig. 1(a) shows a bright field TEM micrograph of $ZF_{10}O$-900, together with the associated selected area diffraction (SAD) pattern, while those of ZF_2O-900 are shown in Fig. 1(b). In both nanohybrids, zinc ferrite and ferrite-related phases occur as more or less spherical nanoparticles, which are uniformly dispersed in the silica matrix. There is little difference between the two nanohybrids, although the nanoparticles in $ZF_{10}O$-900 (10.45 ± 2.07 nm) are slightly larger than those in ZF_2O-900 (9.67 ± 1.74 nm). However, a significant difference is observed in their SAD patterns. As shown in Fig. 1(b), the well-defined rings in the SAD pattern of ZF_2O-900 can be assigned to the crystal planes of the $ZnFe_2O_4$ phase, indicating the established crystallinity of the $ZnFe_2O_4$ particles. In contrast, $ZF_{10}O$-900 exhibits a much more diffuse SAD pattern, although the faint diffraction rings can also be assigned to zinc ferrite of spinel structure, suggesting that the crystallite size of zinc ferrite is much smaller than the particle size shown by TEM.

The fundamental differences between the two nanohybrids are further clearly demonstrated by XRD studies for phase analysis. Well-defined diffraction peaks, all corresponding to $ZnFe_2O_4$ of spinel structure, were observed for ZF_2O-900, as shown in Fig. 2. However, the diffraction peaks observed for

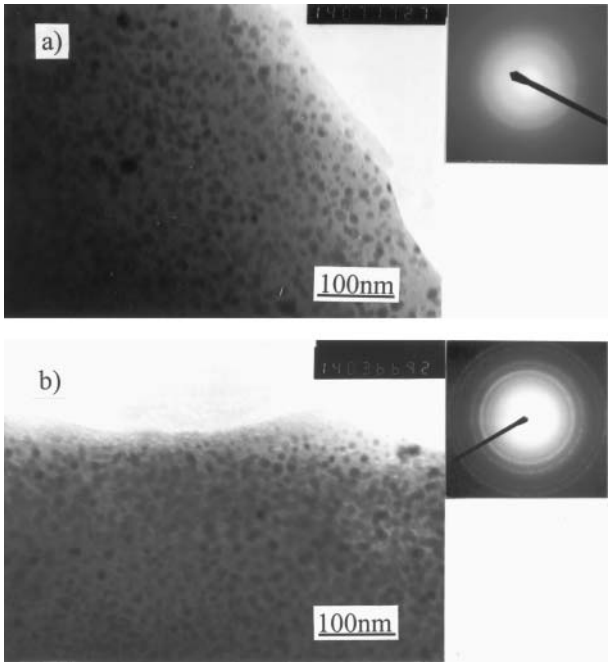

Fig. 1 TEM micrographs and selected area diffraction (SAD) patterns of (a) $ZF_{10}O$-900 and (b) ZF_2O-900.

$ZF_{10}O$-900 are much weaker and broadened. Applying Scherrer's equation to the FWHM of these diffraction peaks, the average crystallite sizes of zinc ferrite in ZF_2O-900 and $ZF_{10}O$-900 were calculated to be 10.0 and 3.3 nm, respectively. The former is consistent with what has been observed using TEM, suggesting that the particles in Fig. 1(b) are discrete crystallites of zinc ferrite. In contrast, the crystallite size for $ZF_{10}O$-900 is much smaller than the particle size observed in Fig. 1(a). In monitoring the phase formation process of zinc ferrite in silica with increasing temperature, only a very broad peak at $2\theta \approx 20°$, attributed to the amorphous nature of the silica gel, was observed in the XRD trace for $ZF_{10}O$-600 [Fig. 2(d)]. No other diffraction peaks were detected over the whole 2θ range investigated, from 20 to 70°. Our previous studies,[15] however, showed that zinc ferrite of spinel structure was readily developed in ZF_2O at 600 °C. In contrast, zinc ferrite of spinel structure was observed to nucleate in the silica matrix of $ZF_{10}O$ at 800 °C, as indicated by the appearance of the weak and broad peaks at 2θ 35.3, 29.9 and 62.2°, as shown

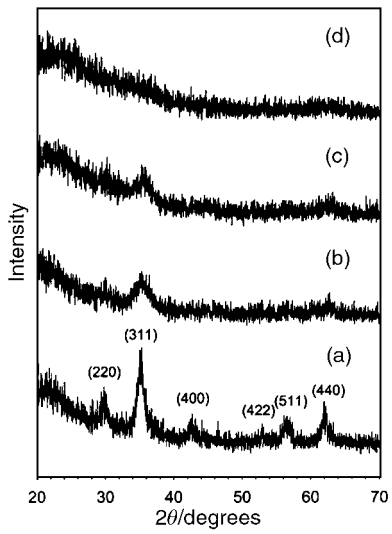

Fig. 2 XRD traces for ZF_2O annealed at (a) 900 °C and $ZF_{10}O$ annealed at (b) 900, (c) 800 and (d) 600 °C.

in Fig. 2(c). When the annealing temperature was further raised, little change was observed in the XRD trace for $ZF_{10}O$-900, implying a slow growth of the spinel crystallites. No other crystalline phase, such as α-Fe_2O_3, ZnO, Fe_2SiO_4 or Zn_2SiO_4, was detected with increasing temperature. The above observations clearly indicate that the rise in Fe/Zn molar ratio from 2 to 10 disfavours the formation of spinel zinc ferrite crystallites in the silica matrix. As will be discussed later, the high Fe/Zn ratio gives rise to a cluster glass structure in the nanoparticles, where nanocrystallites of zinc ferrite occur in amorphous Fe-rich pockets. As such, the peak intensity of zinc ferrite was enhanced and at the same time α-Fe_2O_3 started to appear, when the nanohybrid composition was annealed at 1000 °C. Such a crystallisation temperature is unusually high for α-Fe_2O_3.[16]

γ-Fe_2O_3 exhibits a similar spinel structure to that of zinc ferrite and therefore XRD may not effectively distinguish the two. To check whether the γ-Fe_2O_3 phase occurred in the nanohybrid discussed above, $ZF_{10}O$-900 was further examined by Raman spectroscopy. In the Raman spectrum obtained for $ZF_{10}O$-900, the peaks at 360, 495 and 680 cm^{-1} are at exactly the same positions as the characteristic peaks for $ZnFe_2O_4$,[17] suggesting that the zinc ferrite formed in the silica possesses a $ZnFe_2O_4$ spinel structure. The broad nature of these observed Raman peaks is consistent with the fine crystallinity of the ferrite phase, as has been shown by XRD. Although most of the Raman peaks for zinc ferrite are close to those of γ-Fe_2O_3, the latter exhibits much stronger peaks at 1378 and 1576 cm^{-1}.[18] The absence of these peaks over the range 800–2000 cm^{-1} rules out the possibility of any γ-Fe_2O_3 being present.

Fig. 3 shows the hysteresis loop of the nanohybrid derived from an Fe/Zn molar ratio of 10 ($ZF_{10}O$-900) as measured at 5 K, which exhibits several interesting features. At high fields, the magnetisation increases almost linearly with the applied magnetic field and shows a lack of magnetic saturation, even at very high magnetic fields, which is characteristic of antiferromagnetism or paramagnetism. At low fields, the rapid change in demagnetisation and remagnetisation with applied magnetic field can be attributed to the existence of a ferrimagnetic phase. The slight narrowing in the hysteresis loop along the magnetisation axis at low applied fields is due to the spin-flop transition of an antiferromagnetic phase.[19] These magnetic behaviours clearly demonstrate the occurrence of a mixture of two different phases: ferrimagnetic crystallite clusters of zinc ferrite and antiferromagnetic iron-rich pockets of amorphous structure in the silica matrix. Magnetisation of $ZF_{10}O$-900 as a function of measurement temperature during zero-field cooling (ZFC) and field cooling (FC) at an applied field of 0.05 T is shown in the inset of Fig. 3. For zero-field-cooling, a maximum magnetisation occurs at the cluster glass freezing temperature, T_f, around 50 K. The presence of irreversibility (*i.e.*, the differences between the ZFC and FC curves) below a temperature close to T_f is a characteristic behaviour of cluster

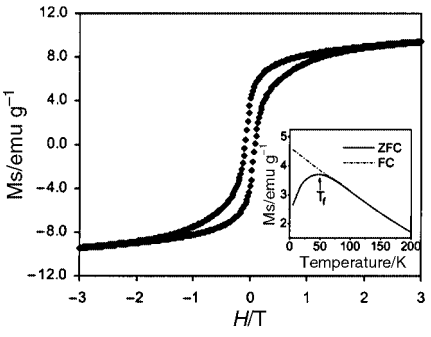

Fig. 3 Hysteresis loop for $ZF_{10}O$-900 measured at 5 K. Insert is the zero-field-cooled (ZFC) and field-cooled (FC) curves with an applied field of 0.05 T for the same sample.

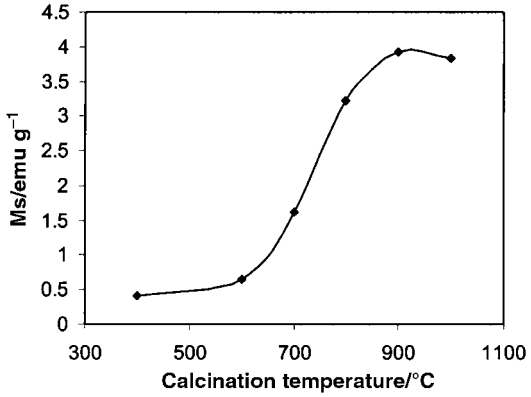

Fig. 4 Saturation magnetization (M_s) measured at room temperature for nanohybrids having an Fe/Zn ratio of 10 annealed at different temperatures.

glasses.[20–22] The initial rise in magnetisation at temperatures lower than T_f is due to the influence of the antiferromagnetic iron-rich amorphous pockets on the overall magnetic behaviour.[23–25]

Fig. 4 illustrates the saturation magnetisation (M_s) measured at room temperature for $ZF_{10}O$ annealed at different temperatures. Due to the lack of magnetic saturation at high magnetic field, the values of M_s reported in the following discussion refer to the magnetic moment at the highest available field (5 T) employed in our laboratory. There is little increase in saturation magnetisation at temperatures up to 600 °C. When the annealing temperature is raised from 600 to 900 °C, M_s increases, apparently as a result of the nucleation and growth of the zinc ferrite clusters in Fe-rich pockets. It reaches a maximum of 3.9 emu g^{-1} at 900 °C. Further increasing the annealing temperature to 1000 °C led to a fall in the saturation magnetisation. These results are in line with what has been shown by phase analysis of XRD and Raman data. As mentioned earlier, the antiferromagnetic α-Fe_2O_3 phase started to develop in the iron-rich pockets when annealed at 1000 °C. A strong interaction between α-Fe_2O_3 and zinc ferrite crystallites causes a depression in the overall saturation magnetisation at 1000 °C. Similar interactions were observed by Cannas *et al.*,[11] who noted a depression in magnetisation when α-Fe_2O_3 was formed in the γ-Fe_2O_3–SiO_2 nanohybrids.

Stoichiometric zinc ferrite ($ZnFe_2O_4$) exhibits a normal spinel structure, which possesses antiferromagnetic behaviour. The above-observed ferrimagnetism of $ZF_{10}O$-900 can be attributed to the replacement of Zn^{2+} cations in tetrahedral A sites by Fe^{3+} cations in the spinel structure at a high enough Fe/Zn molar ratio, which was observed in the IR spectroscopy studies discussed below, resulting in stronger A–B coupling interactions. Fig. 5 shows the hysteresis loops measured at room temperature for nanohybrids derived from various Fe/Zn molar ratios. The inset illustrates the increase in magnetisation with rising Fe/Zn molar ratio, which slows down at Fe/Zn molar ratios above 5. This is consistent with the observation that a cluster glass structure occurs in the nanohybrids, where zinc ferrite crystallites coexist with the antiferromagnetic Fe-rich pockets in the silica matrix. Accordingly, the increase in magnetization slows down at very high Fe/Zn molar ratios. It was also noted in this work that the magnetisation varied with cooling rate after annealing. For instance, $ZF_{10}O$-900 in Fig. 5, which was quenched in air after annealing at 900 °C, has an M_s of 8.8 emu g^{-1}, compared to 3.9 emu g^{-1} for $ZF_{10}O$-900 in Fig. 4, which was cooled to room temperature at a cooling rate of 2 °C min^{-1}. This can be attributed to a strong A–B coupling interaction caused by a large number of Fe^{3+} occupancies in the tetrahedral A sites at the high cooling rate.[26,27]

In order to understand the origin of the above-discussed cluster glass structure, nanohybrids derived from an Fe/Zn

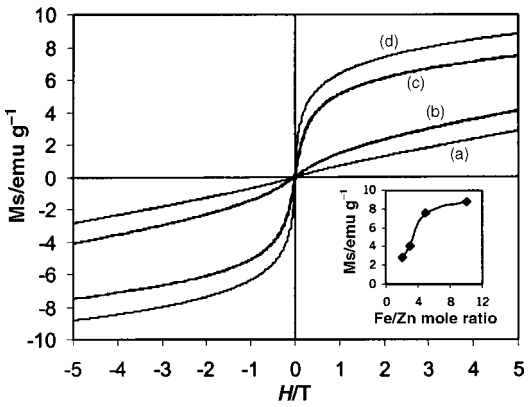

Fig. 5 Hysteresis loops measured at room temperature for (a) ZF_2O-900, (b) ZF_3O-900, (c) ZF_5O-900 and (d) $ZF_{10}O$-900, quenched in air. Inset shows magnetization as a function of Fe/Zn molar ratio.

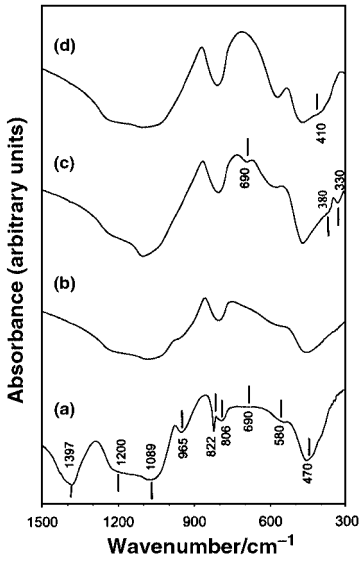

Fig. 6 FT-IR spectra of $ZF_{10}O$ dried at room temperature (a) and then annealed at (b) 600 or (c) 900 °C. The spectrum of ZF_2O annealed at 900 °C (d) is also shown for comparison.

ratio of 10 and annealed at various temperatures were analysed using infrared spectroscopy. As shown in Fig. 6, strong absorption bands at 470, 806 and 1089 cm^{-1} occur, along with a shoulder at 1200 cm^{-1}, which can be attributed to characteristic vibrations of Si–O–Si bridges in the silica network.[28–30] The bands at 1397 and 822 cm^{-1} observed for the gel dried at room temperature are due to vibrations corresponding to NO_3^-,[28,31] and disappear at high temperatures as a result of the decomposition and elimination of nitrate species. The band at 965 cm^{-1}, which can be attributed to either the Si–O–H stretching vibration or a Si–O–Fe vibration, or both,[30,32] is weakened with increasing annealing temperature and disappears in the spectrum at 900 °C, indicating the elimination of physically absorbed water and the break up of Fe–O stretching in the Si–O–Fe bond. The O–Fe stretching in the Si–O–Fe bond also results in the occurrence of a minor band at around 580 cm^{-1},[28,33] which is already weakened at 600 °C. It is, however, recovered at 900 °C, due to the emergence of the characteristic Fe–O band for zinc ferrite clusters.[34,35] An additional band characteristic of zinc ferrite clusters due to the stretching vibration of Zn–O appears at around 410 cm^{-1} at 900 °C. The band at around 330 cm^{-1} is assigned to the displacement of Zn^{2+} cations in A sites by Fe^{3+} cations.[34] The rather faint band at around 690 cm^{-1} observed at low temperatures becomes much stronger at 900 °C, very likely due to the interaction between Zn^{2+} and the silica glass network, which can result in bands between the two characteristic bands for silica at 800 and 470 cm^{-1}.[31,36] Similar bands were observed as a result of the interaction between Ni^{2+} or Cu^{2+} and the silica network.[31,36,37] For comparison purposes, the IR spectrum of ZF_2O-900 is included in Fig. 6. As expected, the two characteristic bands of zinc ferrite are much stronger in ZF_2O-900 than in $ZF_{10}O$-900. That at 410 cm^{-1}, originally observed for ZF_2O-900, is shifted to 380 cm^{-1} for $ZF_{10}O$-900. Shifts have also been observed for the infrared bands corresponding to $NiFe_2O_4$ due to changes in the ferrite stoichiometry.[38] The bands at 330 and 690 cm^{-1}, associated with the substitution of Zn^{2+} by Fe^{3+}, and the interaction between Zn^{2+} and the silica matrix, respectively, are, however, not detected for ZF_2O-900.

The TGA measurement in this work indicated that $Fe(NO_3)_3$ decomposed at a lower temperature than did $Zn(NO_3)_2$. On the basis of the XRD, TEM and FT-IR results discussed above, the formation of zinc ferrite in silica at an Fe/Zn ratio of 10 can be represented schematically, as in Fig. 7. In the as-dried alcogel, Zn^{2+} and Fe^{3+} are randomly distributed in the amorphous network of silica, as shown by the interactions between these cations and the silica network observed in the IR spectra. With increasing annealing temperature, the decomposition of iron nitrate and subsequent break up of Si–O–Fe bonds frees the

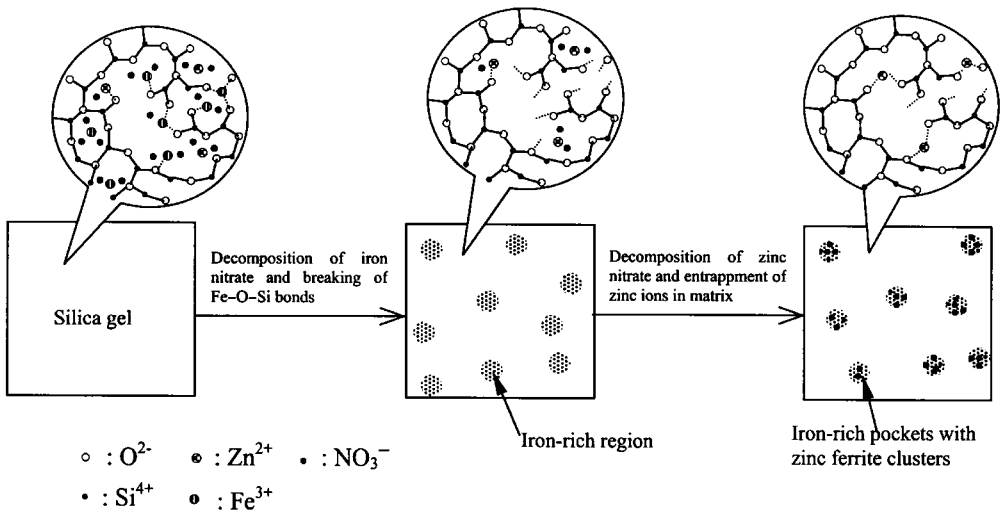

Fig. 7 A schematic representation of the formation process of the zinc ferrite/SiO_2 nanohybrids.

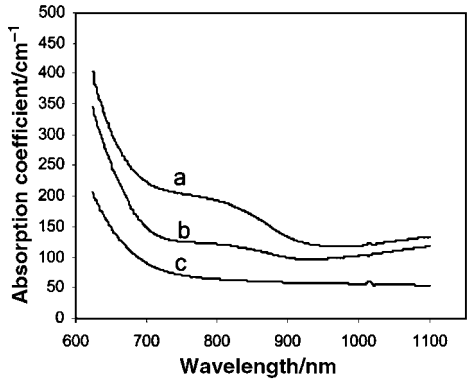

Fig. 8 Absorption spectra for (a) ZF_2O-900, (b) ZF_3O-900, and (c) $ZF_{10}O$-900.

Fe^{3+} in the network, leading to Fe-rich pockets in the silica matrix. As a result of the release of Fe^{3+} cations, the negatively charged dangling Si–O– bonds can entrap Zn^{2+} cations obtained from the decomposition of $Zn(NO_3)_2$ at elevated temperatures. The entrapment of Zn^{2+} by the silica network is demonstrated by the appearance of a strong Zn^{2+}–silica interaction at 690 cm^{-1} for $ZF_{10}O$-900, which was not observed for ZF_2O-900. The deficiency of Zn^{2+} in the Fe-rich pockets limits the number of zinc ferrite crystallites that can be nucleated and grown. Furthermore, the presence of these zinc ferrite crystallites, together with the confinement of the silica matrix, suppresses the nucleation and growth of α-Fe_2O_3. Suppression of nucleation and growth of α-Fe_2O_3 by the introduction of foreign cations has been reported previously.[39,40] This accounts for the unusually high crystallisation temperature (1000 °C) observed for α-Fe_2O_3 in the nanohybrid when the Fe/Zn ratio is controlled at 10. While the iron-rich pockets remain amorphous at temperatures as high as 900 °C, the cluster glass structure results.

Fig. 8 shows the absorption spectra of zinc ferrite–silica nanohybrids derived from three different Fe/Zn ratios, that is Fe/Zn = 2, 3, and 10. The absorption coefficient of all three compositions remains below 400 cm^{-1} in the "red" spectral region from 620 nm. They are therefore considerably more transparent, at least to red visible light, than the transparent magnetic γ-Fe_2O_3–polymer nanohybrid, synthesised by Ziolo *et al.*[4] These investigators observed an absorption coefficient in the range 10^3 to 10^4 cm^{-1}, which is about an order of magnitude higher than what has been found in this work. It is also of interest to note in Fig. 8 that ZF_2O-900 exhibits a small absorption edge at 800 nm, which is weakened with increasing Fe/Zn ratio. This is due to the change in structure as the cluster glass structure is developed with increasing Fe/Zn ratio. A further sharp absorption edge is observed at around 600 nm, with a slight blue shift when the Fe/Zn ratio becomes 10. It is known that the correlation between absorption coefficient α

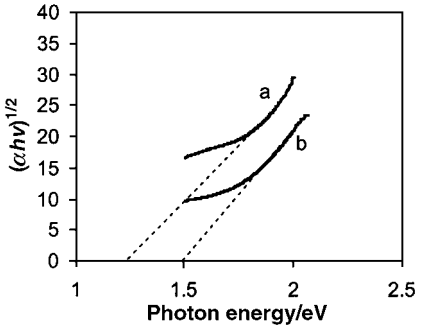

Fig. 9 Relation between $(\alpha hv)^{1/2}$ and photon energy hv for (a) ZF_2O-900 and (b) $ZF_{10}O$-900.

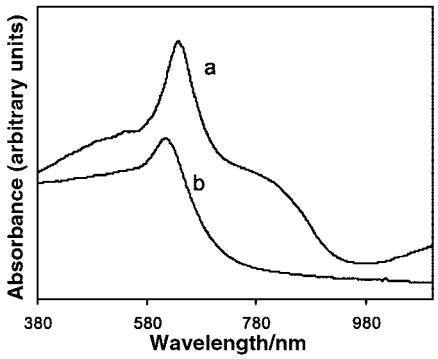

Fig. 10 Absorption spectra for (a) ZF_2O-900 and (b) $ZF_{10}O$-900, with 96% of the incident light passing through the sample.

and optical band gap E_g for fine particles obeys the following equation:[41]

$$(\alpha hv)^{1/2} = A(hv - E_g)$$

where A and hv are the edge-width parameter and photon energy, respectively. Hence, the optical band gap for the absorption peak can be obtained by extrapolating the linear portion of the plot of $(\alpha hv)^{1/2}$ *versus* hv to α=0, as shown in Fig. 9 for ZF_2O-900 and $ZF_{10}O$-900. The values of E_g for ZF_2O-900 and $ZF_{10}O$-900 are calculated to be 1.25 and 1.5 eV, respectively. Therefore, the absorption edge is blue-shifted by 0.25 eV when the Fe/Zn ratio is increased from 2 to 10.

Although the absorbance in the low wavelength region was not measured directly in this work, an experiment was conducted by allowing 96% of the incident light to pass through the nanohybrid while the remaining beam was directed onto the detector. The resulting absorption spectra, as shown in Fig. 10, exhibit a similar trend in the high wavelength range to that shown in Fig. 8. The sharp absorption edge in the latter appears as an absorption peak at 600 nm in Fig. 10, indicating a high absorption of yellow light. Such a unique feature is technologically useful for photochemical processes, such as photocatalysis and photochemical production of hydrogen from water.[42] Their absorption coefficients remain relatively low in value over the rest of the visible region.

IV Conclusions

The structure and magnetic and optical properties of zinc ferrite–silica nanohybrids derived from an *in situ* sol–gel route are strongly affected by the Fe/Zn molar ratio. A fundamentally different cluster glass structure was revealed by magnetic characterisation and studies using XRD, Raman and TEM at an Fe/Zn ratio of 10. In the highly Zn^{2+} deficient environment, nucleation and crystallisation of α-Fe_2O_3 was suppressed to a temperature above 900 °C by the occurrence of zinc ferrite crystallites of spinel structure and the confinement of the silica matrix, resulting in the cluster glass structure. The Fe/Zn molar ratio also affects the optical properties of the nanohybrids. The high absorption edge in the yellow visible light region is blue-shifted by 0.25 eV when the Fe/Zn ratio increases from 2 to 10.

References

1 V. Raul, *Magnetic Ceramics*, Cambridge University Press, Cambridge, UK, 1994.
2 L. L. Beecroft and C. K. Ober, *Chem. Mater.*, 1997, **9**, 1302.
3 A. Yasumori, H. Matsumoto, S. Hayashi and K. Okada, *J Sol–Gel Sci. Technol.*, 2000, **18**, 249.
4 R. F. Ziolo, E. P. Giannelis, B. A. Weinstein, M. P. O'Horo, B. N. Ganguly, V. Mehrotra, M. W. Russell and D. R. Huffman, *Science*, 1992, **257**, 219.
5 B. H. Sohn, R. E. Cohen and G. C. Papaefthymiou, *J. Magn. Magn. Mater.*, 1998, **182**, 216.

6 C. Castro, J. Ramos, A. Millan, J. G. Calbet and F. Palacio, *Chem. Mater.*, 2000, **12**, 3681.
7 F. D. Monte, M. P. Morales, D. Levy, A. Fernandez, M. Ocana, A. Roig, E. Molins, K. O'Grady and C. J. Serna, *Langmuir*, 1997, **13**, 3627.
8 F. Bentivegna, J. Ferre, M. Nyvlt, J. P. Jamet, D. Imhoff, M. Canva, A. Brun, P. Veillet, S. Visnovsky, F. Chaput and J. P. Boilot, *J. Appl. Phys.*, 1998, **83**, 7776.
9 V. Papaefthymiou, A. Kostikas, A. Simopoulos, D. Niarchos, S. Gangopadyay, G. C. Hadjupaayis, C. M. Sorensen and K. J. Kablunde, *J. Appl. Phys.*, 1990, **67**, 4487.
10 F. Bentivegna, J. Ferre, M. Nyvlt, J. P. Jamet, A. Brun, S. Visnovsky and R. Urban, *J. Appl. Phys.*, 1999, **85**, 2270.
11 C. Cannas, D. Gatteschi, A. Musinu, G. Piccaluga and C. Sangregorio, *J. Phys. Chem. B*, 1998, **102**, 7721.
12 S. Bruni, F. Cariati, M. Casu, A. Lai, A. Musinu, G. Piccaluga and S. Solinas, *Nanostruct. Mater.*, 1999, **11**, 573.
13 M. Casu, F. C. Marincola, A. Lai, A. Musinu and G. Piccaluga, *J Non-Cryst. Solids*, 1998, **232–234**, 329.
14 L. Li, G. Li, R. L. Smith and H. Inomata, *Chem. Mater.*, 2000, **12**, 3705.
15 Z. H. Zhou, J. M. Xue, H. S. O. Chan and J. Wang, *J. Appl. Phys.*, 2001, **90**, 4169.
16 R. M. Cornell and U. Schwertmann, *The Iron Oxides*, VCH, Weinheim, Germany, 1996.
17 M. H. Sousa, F. A. Tourinho and J. C. Rubim, *J. Raman Spectrosc.*, 2000, **31**, 185.
18 D. L. A. de Faria, S. V. Silva and M. T. de Oliveira, *J. Raman Spectrosc.*, 1997, **28**, 873.
19 J. Lago, P. D. Battle and M. J. Rosseinsky, *J. Phys.: Condens. Matter*, 2000, **12**, 2505.
20 J. Feng and L. Hwang, *Appl. Phys. Lett.*, 1999, **75**, 1592.
21 P. A. Joy and S. K. Date, *J. Magn. Magn. Mater.*, 2000, **218**, 229.
22 Y. Sun, X. Xu, W. Tong and Y. Zhang, *Appl. Phys. Lett.*, 2000, **77**, 2734.
23 J. Vergara, R. J. Ortega-Hertogs, V. Madurga, F. Sapina, Z. El-Fadli, E. Martinez, A. Beltran and K. V. Rao, *Phys. Rev. B*, 1999, **60**, 1127.
24 J. A. Alonso, M. J. Martínez-Lope, M. T. Casais, J. L. Martínez and M. T. Fernández-Díaz, *Chem. Mater.*, 2000, **12**, 1129.
25 D. V. Dimitrov, K. Unruh, G. C. Hadjipanayis, V. Papaefthymiou and A. Simopoulos, *Phys. Rev. B*, 1999, **59**, 14499.
26 L. L. Hench and J. K. West, *Principles of Electronic Ceramics*, John Wiley & Sons, Toronto, Canada, 1990, p. 316.
27 K. Tanaka, M. Makita, Y. Shimizugawa, K. Hirao and N. Soga, *J. Phys. Chem. Solids*, 1998, **59**, 1611.
28 S. Bruni, F. Cariati, M. Casu, A. Lai, A. Musinu, G. Piccaluga and S. Solinas, *Nanostruct. Mater.*, 1999, **11**, 573.
29 E. J. Kamitsos and A. P. Patsis, *Phys. Rev. B*, 1993, **48**, 12499.
30 H. Izutsu, P. K. Hair, Y. Kiyozumi and F. Mizwkami, *Mater. Res. Bull.*, 1997, **32**, 1303.
31 O. Clause, M. Kermarec, L. Bonneviot, F. Villain and M. Che, *J. Am. Chem. Soc.*, 1992, **114**, 4709.
32 A. Albawahe, S. E. Friberg, J. Sjoblom and G. Farrington, *J. Dispersion Sci. Technol.*, 1998, **19**, 613.
33 C. M. Wang and H. Chen, *Phys. Chem. Glasses*, 1981, **28**, 39.
34 X. Li, G. Lu and S. Li, *J. Alloys Compd.*, 1996, **235**, 150.
35 J. Preudhomme and P. Tarte, *Spectrochim. Acta, Part A*, 1971, **27**, 961.
36 A. M. Klonkowski, B. Grobelna, T. Widernik, A. Jankowska-Frydel and W. Mozgawa, *Langmuir*, 1999, **15**, 5814.
37 L. Li, G. Li, R. L. Smith and H. Inomata, *Chem. Mater.*, 2000, **12**, 3705.
38 A. A. Kamnev and M. Ristic, *J. Mol. Struct.*, 1997, **408–409**, 301.
39 Q. Y. Liu and K. Osseo-Asare, *J. Colloid Interface Sci.*, 2000, **231**, 401.
40 T. Zhang, P. Hing and R. Zhang, *J. Mater. Sci.*, 2000, **35**, 1419.
41 G. Mills, Z. Li and M. Dan, *J. Phys. Chem.*, 1988, **92**, 822.
42 J. Liu, G. Lu, H. He, H. Tan, T. Xu and K. Xu, *Mater. Res. Bull.*, 1996, **31**, 1049.